Available online at www.sciencedirect.com

ScienceDirect

Acta Materialia 61 (2013) 7543–7554

Acta MATERIALIA

www.elsevier.com/locate/actamat

Elastic properties of single-crystalline ω phase in titanium

M. Tane [a,*], Y. Okuda [a], Y. Todaka [b], H. Ogi [c], A. Nagakubo [c]

[a] The Institute of Scientific and Industrial Research, Osaka University, Ibaraki, Osaka 567-0047, Japan
[b] Department of Mechanical Engineering, Toyohashi University of Technology, Toyohashi, Aichi 441-8580, Japan
[c] Graduate School of Engineering Science, Osaka University, Toyonaka, Osaka 560-8531, Japan

Received 31 July 2013; received in revised form 13 August 2013; accepted 13 August 2013
Available online 30 September 2013

Abstract

The elastic properties of single-crystalline ω (hexagonal) phase of titanium are studied. Understanding the elastic properties is important for the development of biomedical titanium alloys with a low Young's modulus. However, the elastic properties of the ω phase have remained unclear because of the difficulty in preparing a large single crystal consisting of a single phase of the ω phase, even though the ω phase has been believed to exhibit a higher elastic modulus than the β (body-centered cubic) phase. In this work, pure titanium was severely deformed by high-pressure torsion processing, to obtain polycrystalline specimens consisting exclusively of the ω phase, which is metastable at room temperature. For the ω-phase polycrystal, the complete set of elastic stiffness components was measured by RUS combined with laser Doppler interferometery. By analyzing the elastic stiffness of the ω-phase polycrystal on the basis of an inverse Voigt–Reuss–Hill approximation, the elastic stiffness components of the single-crystalline ω phase were determined. The Young's modulus of the ω phase along $\langle 0001 \rangle$ was found to be clearly higher than that along $\langle 11\bar{2}0 \rangle$, and the shear modulus also exhibited anisotropy. Importantly, the Young's modulus and shear modulus of the metastable ω phase were higher than those of the β phase and also higher than those of the α (hexagonal close-packed) phase, which is stable at room temperature. Furthermore, analysis by a micromechanics model using the determined elastic stiffness deduced the effect of ω phase formation on the elastic properties of β-phase titanium alloys.

Keywords: Elastic properties; Titanium; Omega phase; Acoustic methods; Biomaterials

1. Introduction

Titanium and its alloys are important structural and biomedical materials [1]. Thus, their various properties and phase transformations have been investigated extensively [2–7]. Recently, the elastic properties of β-phase Ti alloys with a body-centered cubic (bcc) lattice have attracted considerable attention because their Young's modulus is quite low. A low Young's modulus is necessary for hard tissue replacements such as artificial hip joints and dental implants, to prevent bone degradation and the absorption caused by the difference between the Young's moduli of the replacement and natural human bone [8]. Thus far, the elastic properties of various β-phase Ti alloys composed of non-toxic elements have been investigated, e.g., Ti–Nb–Ta–Zr [9], Ti–Nb–Zr–Sn [10], Ti–Nb–Zr [11] and Ti–Nb–Ta–Zr–O [12].

To achieve a low Young's modulus in β-phase Ti alloys, decreasing their β phase stability is quite important [13–16]. However, there is a lower limit of the β phase stability for achieving a low Young's modulus. This is because the formation of the ω (hexagonal) phase, which appears in the low-stability β phase, is believed to increase the Young's modulus, assuming that the ω phase exhibits a higher elastic modulus than the β phase. However, only the bulk modulus of polycrystalline ω phase, which was measured under high pressure, has been reported [17–19], because of the difficulty in preparing a specimen consisting of a single phase of the ω phase under ambient pressure. Thus, the other elastic properties have remained unclear. The present study focuses on the elastic properties of the

* Corresponding author. Tel.: +81 6 6879 8437; fax: +81 6 6879 8439.
E-mail address: mtane@sanken.osaka-u.ac.jp (M. Tane).

1359-6454/$36.00
http://dx.doi.org/10.1016/j.actamat.2013.08.036

ω phase, which are useful for understanding the effect of the ω phase formation on the elastic properties of Ti alloys, even though the α'' (orthorhombic) martensite phase is also formed in the low-stability β phase. It is well known that the ω phase is formed by quenching from high temperature (athermal ω phase), by annealing (isothermal ω phase) and by deformation of the low-stability β phase [16,20–26]. The ω phase has a hexagonal lattice with three atoms per unit cell, and their ideal atomic positions are at (0, 0, 0), (1/3, 2/3, 1/2) and (2/3, 1/3, 1/2), respectively.

To analyze the effect of ω phase formation on the Young's modulus of Ti alloys in detail, it is essential to clarify the elastic properties of single-crystalline ω phase. Understanding the elastic properties of the single crystal is also helpful for comprehending the phase transformation and mechanical properties of the ω phase, which have remained unclear. However, the preparation of a specimen consisting of a single phase of ω-phase single crystal has never been successful. Therefore, the elastic properties of the ω-phase single crystal, i.e., the five independent elastic stiffness components of the hexagonal elastic symmetry have never been measured. So far, some papers have only reported the elastic properties of single-crystalline ω phase, estimated by first-principles (FP) calculations based on density functional theory (DFT) [27–29]. However, the values have not been validated by comparison with measured values.

In the present paper, the elastic properties of single-crystalline ω phase in pure titanium were studied. Pure α-phase titanium was severely deformed by a high-pressure torsion (HPT) processing [30–33] to obtain polycrystalline specimens consisting of a single phase of the ω phase, which was metastable at room temperature under ambient pressure. The texture and microstructure of the ω phase formed by the HPT process were analyzed by X-ray diffraction (XRD), through X-ray pole figures and by transmission electron microscopy (TEM). Taking into account the texture and microstructure, a complete set of elastic stiffness components of the ω-phase polycrystal were measured with resonant ultrasound spectroscopy (RUS) [34] combined with laser Doppler interferometery (LDI) [35] and electromagnetic acoustic resonance (EMAR) [36]. By analyzing the elastic stiffness of the ω-phase polycrystal on the basis of a recently developed inverse Voigt–Reuss–Hill approximation [37], the elastic stiffness components of the single-crystalline ω phase were determined. The elastic properties of the single-crystalline ω phase obtained were systematically compared with those obtained by FP calculations [29] and with the elastic properties of the α and β phases [38–40]. Furthermore, for β-phase Ti alloys, the effect of the ω phase formation on the elastic properties was analyzed using the elastic properties of the ω-phase single crystal obtained, based on a micromechanics model [41] consisting of Eshelby's inclusion theory [42], Mori–Tanaka's mean-field theory [43] and Bruggeman's effective-medium approximation [44].

2. Experimental

Pure α-phase Ti ingots, which contained Fe (330 ppm) and O (450 ppm) as impurities, were used as raw materials. The raw-material ingots were annealed at 1073 K for 3.6 ks in Ar atmosphere, to homogenize their microstructures. The annealed ingots were cut into disk specimens 20 mm in diameter and 0.85 ± 0.01 mm thick. The prepared disk specimens were severely deformed by the HPT process at room temperature to achieve the transformation from α to ω phase [30–33]. A disk specimen was held between two anvils under a compressive pressure (P) of 5 GPa, and the two anvils were rotated 10 times at a relative rotation speed of 0.2 rpm. The amount of applied shear strain (γ) is given by $\gamma = 2\pi Nr/t$ [31], where r is the distance from the center of the disk specimen, t ($=0.85 \pm 0.01$ mm) is the thickness of the disk specimen, and $N(=10)$ is the number of rotations. By the HPT process, severe plastic deformation was applied to the disk specimens and the deformed disk specimens ~20 mm in diameter and ~0.4–0.5 mm in thickness consisting of ω-phase polycrystals were prepared. The coordinate system for the disk specimen is shown in Fig. 2, where the x_3 axis is parallel to the thickness direction. The microstructure and phase constitution of the deformed specimens consisting of the ω-phase polycrystals were analyzed by TEM (JEM-2100F, JEOL: 200 kV). The phase constitution of the deformed specimens was also analyzed by XRD (Rigaku smartLab: Cu K_α radiation). The texture formed by the HPT process was analyzed by X-ray pole figures (Rigaku smatLab: Cu K_α radiation).

For a plate or disk-shaped specimen, it is difficult to determine the elastic stiffness components c_{33}, c_{44} and c_{55} using RUS combined with LDI. The elastic stiffness components c_{33}, c_{44} and c_{55} correspond to the longitudinal and two transverse elastic waves propagating along the thickness direction, respectively. The difficulty in determining these components lies in the fact that the elastic stiffness components hardly contribute to the resonance vibration frequencies of a thin specimen from which elastic stiffness components are determined by RUS. Thus, the c_{33} and c_{44} ($=c_{55}$) components of the ω-phase polycrystal were determined by a thickness resonance method. The deformed disk specimen exhibited transverse isotropy in the plane perpendicular to the thickness (x_3) direction, as described in Section 3.1, and therefore $c_{44} = c_{55}$. The resonance frequencies of the first mode of the longitudinal and transverse elastic waves propagating along the thickness direction were measured by EMAR [36]. The c_{33} and $c_{44}(= c_{55})$ components were determined from the resonance frequencies using the following equations.

$$c_{33} = (2f_L t)^2 \rho, \quad \text{and} \quad c_{44} = (2f_T t)^2 \rho, \tag{1}$$

where f_L and f_T, respectively, are the resonance frequencies of the longitudinal and transverse elastic waves, and t and ρ are the thickness and density of the disk specimen, respectively.

The deformed disk specimens consisting of the ω-phase polycrystals were cut into square specimens using a spark erosion cutting machine, and the dimensions of the samples were $\sim 9 \times 9 \times 0.4$–$0.5\ \mathrm{mm}^3$. The elastic stiffness components, with the exception of c_{33} and c_{44} of the ω-phase polycrystal, were measured by RUS combined with LDI, using the plate-shaped specimens. In the RUS analysis, the c_{33} and c_{44} components were fixed as the average values for seven and five specimens, respectively, determined by the thickness resonance method, and LDI was used to identify the vibrational modes of the resonance peaks measured by RUS [35].

The elastic stiffness components of the single-crystalline ω phase were calculated from the components measured for the ω-phase polycrystal using an inverse Voigt–Reuss–Hill approximation [37], in which the texture and microstructure analyzed by the X-ray pole figure, XRD and TEM were taken into account.

3. Experimental results

3.1. Microstructure and texture formed by the HPT process

Fig. 1a shows a bright-field image of the microstructure in a disk specimen deformed by the HPT process. The observed position was 4 mm apart from the center of the disk specimen. Equiaxed grains of a few hundred nanometers containing many dislocations are evident. Fig. 1b shows a selected-area electron diffraction (SAED) pattern taken from a region ~750 nm in diameter in the bright-field image of Fig. 1a. The electron diffraction pattern indicates that the grains consisted of the ω phase, in agreement with a previous report [31].

Fig. 2 shows the XRD pattern of a deformed disk specimen taken from a specimen surface perpendicular to the thickness (x_3) direction. The large $(10\bar{1}0)$ and/or $(11\bar{2}0)$ peak derived from ω phase, $(10\bar{1}0/11\bar{2}0)_\omega$, was detected; whereas, the other peaks derived from ω phase were fairly small. The $(10\bar{1}0)_\omega$ and $(11\bar{2}0)_\omega$ planes have almost the same interplanar spacings [32], and therefore they cannot be differentiated by XRD analysis. The detection of the large $(10\bar{1}0/11\bar{2}0)_\omega$ peak indicated that the $\langle 10\bar{1}0/11\bar{2}0\rangle$ directions of ω-phase grains were strongly oriented along the thickness direction. For the α phase, only a fairly small peak was detected, which means that the deformed specimens virtually exclusively consisted of the ω phase, consistent with the TEM observations.

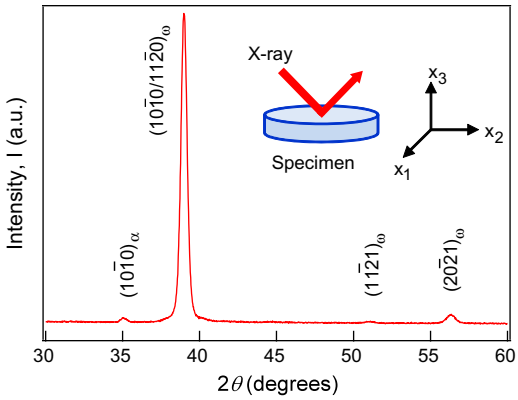

Fig. 2. XRD pattern of a deformed disk specimen taken from the specimen surface perpendicular to the thickness (x_3) direction.

Fig. 3a shows the $(10\bar{1}0/11\bar{2}0)_\omega$ pole figure of the deformed disk specimen taken from the central region of the specimen surface perpendicular to the thickness (x_3) direction. The definition of the angle α is shown in the schematic illustration of Fig. 3c. The high intensity levels at $\alpha = 30°$ and 90° indicated that the $\langle 10\bar{1}0/11\bar{2}0\rangle$ directions of ω-phase crystals were strongly oriented along the thickness (x_3) direction, consistent with results of the XRD analysis. The intensity at $\alpha = 30°$ was circular, with the center located at the center of the pole figure, indicating that the $\langle 0001\rangle$ directions of the ω-phase crystals were isotropically oriented in the plane perpendicular to the thickness (x_3) direction. The $(10\bar{1}0/11\bar{2}0)_\omega$ pole figure, taken from a region apart from the central region, is shown in Fig. 3b, and the position of the analyzed region is shown in

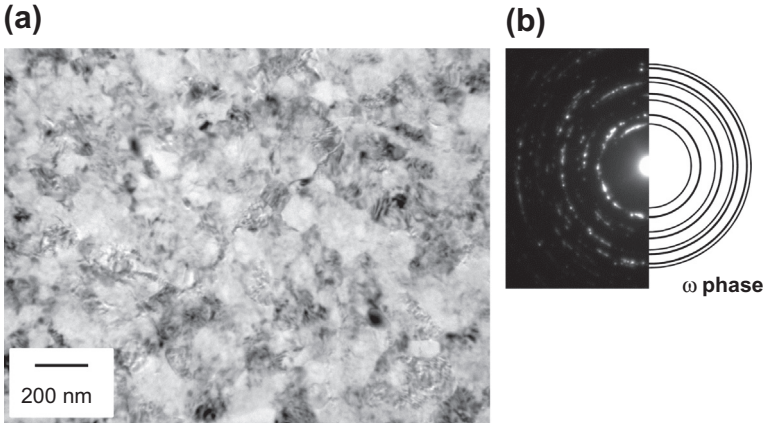

Fig. 1. (a) A bright-field image of the microstructure of a disk specimen deformed by the HPT process and (b) a SAED pattern taken from a region ~750 nm in diameter in the bright-field image of (a). The observed position is 4 mm away from the center of the disk specimen.

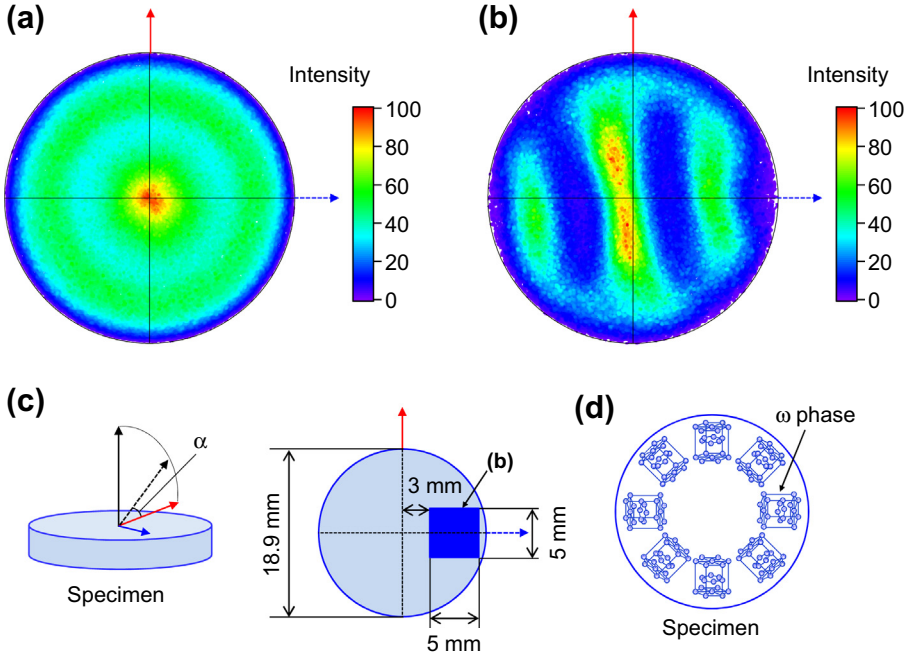

Fig. 3. $(10\bar{1}0)_\omega$ and/or $(11\bar{2}0)_\omega$ pole figures of deformed disk specimens consisting of the ω-phase polycrystal taken from the specimen surfaces perpendicular to the thickness (x_3) direction. The pole figures were taken from (a) the center region of the specimen and (b) a region away from the central region of the specimen. (c) Schematic illustration showing the definition of angle α and position on the specimen surface where the pole figure in (b) was measured. (d) Schematic illustration showing the crystallographic orientation of the ω phase in a disk specimen.

Fig. 3c. The three high-intensity levels were elongated along the direction of the solid arrow. This indicated that the $\langle 0001\rangle_\omega$ directions were oriented along the direction of the dotted arrow. From these two pole figures, it can be deduced that the $\langle 0001\rangle_\omega$ directions were oriented along the radial direction, as shown in the schematic illustration of Fig. 3d. As a result of this $\langle 10\bar{1}0/11\bar{2}0\rangle$ texture, the transverse isotropy was probably realized in the plane perpendicular to the thickness (x_3) direction, i.e., the ω-phase polycrystal exhibited hexagonal elastic symmetry macroscopically, similar to a Nb–Ti/Cu-composite superconductive wire with a concentric arrangement of Nb–Ti fibers in a copper matrix [45].

3.2. Elastic properties of the ω-phase polycrystal

The elastic stiffness components c_{33} and c_{44} in the ω-phase polycrystal were measured by the thickness resonance method using EMAR. The other independent elastic stiffness components of hexagonal elastic symmetry, i.e., c_{11}, c_{12} and c_{13}, were measured by RUS combined with LDI. Table 1 shows the measured c_{ij} components (PC; Meas) and lists the average and standard deviation values for four specimens (c_{11}, c_{12} and c_{13}), seven specimens (c_{33}) and five specimens (c_{44}). The Young's moduli along the directions parallel and perpendicular to the thickness (x_3) direction, $E_{//}$ and $E_\perp$, calculated from the c_{ij} components, are also shown in Table 1. The elastic constants (PC; Meas) exhibited anisotropy of $c_{33} < c_{11}$, $c_{44} < c_{66}$ and $E_{//} < E_\perp$, reflecting the texture formed by the HPT process.

By coordinate conversion of the measured c_{ij} components [46], the orientation dependence of the Young's modulus in the ω-phase polycrystal was calculated. Fig. 4a shows the Young's modulus in directions that were between parallel and perpendicular to the thickness (x_3) direction, where the symbol θ denotes the angle from the thickness direction. The line and error bars denote the average Young's modulus and standard deviations, respectively. The Young's modulus increased monotonically with an increase in the angle θ. The shear modulus also increased with increasing θ, as shown in Fig. 4b. Note that θ is the angle from the shear for the x_2 direction on the x_3 plane with respect to the rotation around the x_1 axis.

4. Determination of elastic properties of ω-phase single crystal by inverse Voigt–Reuss–Hill approximation

4.1. Inverse Voigt–Reuss–Hill approximation

The elastic stiffness components of single-crystalline ω phase were calculated from those of the ω-phase polycrystal using an inverse Voigt–Reuss–Hill approximation [37]. In the application of the inverse Voigt–Reuss–Hill approximation, the $\langle 10\bar{1}0/11\bar{2}0\rangle$ texture in the ω-phase polycrystal was regarded as the $\langle 11\bar{2}0\rangle$ texture. This can be attributed to the elastic equivalence of $\langle 11\bar{2}0\rangle$ and $\langle 10\bar{1}0\rangle$ in the ω phase, which originates from the hexagonal elastic symmetry.

Using the "normal" Voigt approximation [46–48], the effective (macroscopic) elastic stiffness tensor of a textured ω-phase polycrystal C^{pc}_{ijkl} is expressed by an unknown

Table 1
Elastic stiffness components c_{ij} (GPa) and Young's moduli parallel and perpendicular to the thickness (x_3) direction, i.e., $E_{//}$ and $E_{\perp}$ (GPa), respectively, of the ω-phase polycrystal obtained by measurements at RT (PC; Meas); $c_{66} = (c_{11} - c_{12})/2$. Elastic stiffness components c_{ij} (GPa), $E_{//}$, and $E_{\perp}$ (GPa) of the ω-phase polycrystal (PC; Calc) obtained by the Voigt–Reuss–Hill approximation, followed by an inverse Voigt–Reuss–Hill approximation to the elastic stiffness components of ω-phase polycrystal are shown for comparison.

Phase	c_{11}	c_{33}	c_{12}	c_{13}	c_{44}	c_{66}	$E_{//}$	$E_{\perp}$
ω (PC; Meas)	200.8 ± 0.7	177.6 ± 7.3	61.3 ± 1.6	76.6 ± 2.5	56.0 ± 2.0	69.8 ± 0.7	132.7 ± 3.2	162.9 ± 1.3
ω (PC; Calc)	200.9	177.4	61.4	76.7	55.9	69.8	132.5	163.0

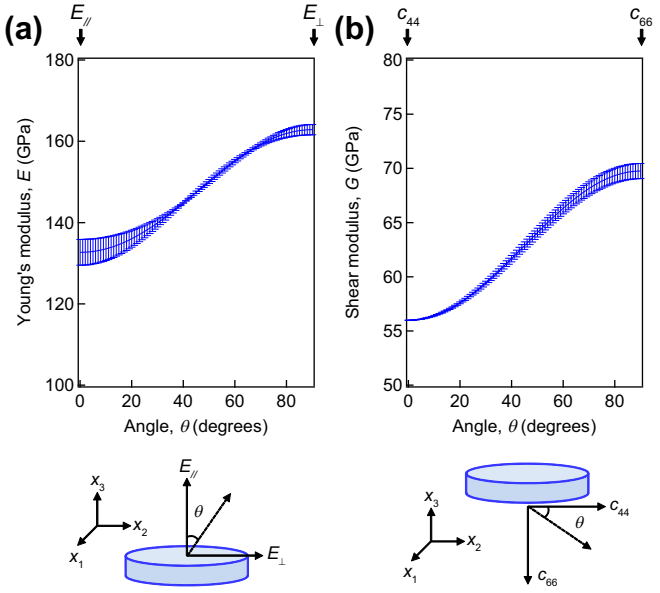

Fig. 4. Orientation dependencies of (a) the Young's modulus and (b) the shear modulus of a deformed specimen consisting of the ω-phase polycrystal between the directions parallel and perpendicular to the thickness (x_3) direction, where θ is: (a) the angle from the x_3 direction and (b) the angle from the shear for the x_2 direction on the x_3 plane with respect to rotation around the x_1 axis. The lines and error bars denote the average and standard deviation values, respectively. The standard deviations reflect the variations in c_{11}, c_{12} and c_{13} for four specimens determined by RUS, because the c_{33} and c_{44} components, determined by the thickness resonance method, were fixed as their average values.

elastic stiffness tensor of the single-crystalline ω-phase C^{sc}_{ijkl}. With the $\langle 11\bar{2}0\rangle$ texture taken into account, the effective elastic stiffness tensor of the textured ω-phase polycrystal is expressed as the orientational average of the elastic stiffness of the single-crystalline ω phase, with respect to rotation around the $\langle 11\bar{2}0\rangle$ direction by the following equation.

$$C^{pc(V)}_{ijkl} = \frac{1}{2\pi}\int_0^{2\pi} a_{ip}a_{jq}a_{kr}a_{ls}C^{sc'}_{pqrs}d\beta, \quad (2)$$

where $C^{sc'}_{ijkl}$ is the elastic stiffness of the single crystal after the coordinate conversion of the elastic stiffness of the single crystal C^{sc}_{ijkl} around the $\langle 10\bar{1}0\rangle$ direction by 90°. After rotation, the $\langle 11\bar{2}0\rangle$ direction is oriented along the x_3 direction. In Eq. (2), the second rank tensor a_{ij} denotes a component for the coordinate conversion around the x_3 axis by the angle β, and the summation convention is applied for the calculation of the equation. The integration and tensor operations in Eq. (2) give the following equation, which calculates the Voigt-approximated effective elastic stiffness matrix of ω-phase polycrystal $c^{pc(V)}_{ij}$ from the elastic stiffness matrix of the single crystal c^{sc}_{ij}:

$$\begin{pmatrix} c^{pc(V)}_{11} \\ c^{pc(V)}_{33} \\ c^{pc(V)}_{12} \\ c^{pc(V)}_{13} \\ c^{pc(V)}_{44} \end{pmatrix} = \begin{pmatrix} \frac{3}{8} & \frac{3}{8} & 0 & \frac{1}{4} & \frac{1}{2} \\ 1 & 0 & 0 & 0 & 0 \\ \frac{1}{8} & \frac{1}{8} & 0 & \frac{3}{4} & -\frac{1}{2} \\ 0 & 0 & \frac{1}{2} & \frac{1}{2} & 0 \\ \frac{1}{4} & 0 & -\frac{1}{4} & 0 & \frac{1}{2} \end{pmatrix} \begin{pmatrix} c^{sc}_{11} \\ c^{sc}_{33} \\ c^{sc}_{12} \\ c^{sc}_{13} \\ c^{sc}_{44} \end{pmatrix}, \quad (3)$$

where the tensor notations $C^{pc(V)}_{ijkl}$ and $C^{sc(V)}_{ijkl}$ are converted to matrix notations $c^{pc(V)}_{ij}$ and $c^{sc(V)}_{ij}$, respectively [49]. The "inverse" matrix of the matrix in Eq. (3) provides the following equation, which calculates the single-crystalline c^{sc}_{ij} from the polycrystalline $c^{pc(V)}_{ij}$:

$$\begin{pmatrix} c^{sc}_{11} \\ c^{sc}_{33} \\ c^{sc}_{12} \\ c^{sc}_{13} \\ c^{sc}_{44} \end{pmatrix} = \begin{pmatrix} 0 & 1 & 0 & 0 & 0 \\ \frac{8}{3} & -\frac{1}{3} & 0 & -\frac{4}{3} & -\frac{8}{3} \\ \frac{1}{3} & \frac{1}{3} & -1 & \frac{4}{3} & -\frac{4}{3} \\ -\frac{1}{3} & -\frac{1}{3} & 1 & \frac{2}{3} & \frac{4}{3} \\ \frac{1}{6} & -\frac{1}{3} & -\frac{1}{2} & \frac{2}{3} & \frac{4}{3} \end{pmatrix} \begin{pmatrix} c^{pc(V)}_{11} \\ c^{pc(V)}_{33} \\ c^{pc(V)}_{12} \\ c^{pc(V)}_{13} \\ c^{pc(V)}_{44} \end{pmatrix}. \quad (4)$$

Similarly, on the basis of the Reuss approximation [46,47,50], the equation for calculating the elastic compliance matrix of the single-crystalline ω phase s^{sc}_{ij} from the Reuss-approximated effective elastic compliance matrix of the ω-phase polycrystal $s^{pc(R)}_{ij}$ can be written as follows.

$$\begin{pmatrix} s^{sc}_{11} \\ s^{sc}_{33} \\ s^{sc}_{12} \\ s^{sc}_{13} \\ s^{sc}_{44} \end{pmatrix} = \begin{pmatrix} 0 & 1 & 0 & 0 & 0 \\ \frac{8}{3} & -\frac{1}{3} & 0 & -\frac{4}{3} & -\frac{2}{3} \\ \frac{1}{3} & \frac{1}{3} & -1 & \frac{4}{3} & -\frac{1}{3} \\ -\frac{1}{3} & -\frac{1}{3} & 1 & \frac{2}{3} & \frac{1}{3} \\ \frac{2}{3} & -\frac{4}{3} & -2 & \frac{8}{3} & \frac{4}{3} \end{pmatrix} \begin{pmatrix} s^{pc(R)}_{11} \\ s^{pc(R)}_{33} \\ s^{pc(R)}_{12} \\ s^{pc(R)}_{13} \\ s^{pc(R)}_{44} \end{pmatrix}. \quad (5)$$

Approximating $c^{pc(V)}_{ij} = c^{meas}_{ij}$ and $s^{pc(R)}_{ij} = s^{meas}_{ij}$ in Eqs. (4) and (5), the Voigt-approximated elastic stiffness of a single crystal $c^{sc(V)}_{ij}$ and the Reuss-approximated elastic compliance of a single crystal $s^{sc(R)}_{ij}$ can be calculated; $c^{meas}_{ij}(=\{s^{meas}_{ij}\}^{-1})$ is the measured elastic stiffness of the ω-phase polycrystal. Similarly to the normal Voigt–Reuss–Hill approximation, proper elastic stiffness of the single

crystal is given by the average of Voigt and Reuss approximations.

$$c_{ij}^{\mathrm{sc(H)}} = \frac{c_{ij}^{\mathrm{sc(V)}} + \{s_{ij}^{\mathrm{sc(R)}}\}^{-1}}{2}. \quad (6)$$

4.2. Elastic properties of single-crystalline ω phase

Table 2 shows the elastic stiffness components of the single-crystalline ω phase at room temperature (RT), determined by the inverse Voigt–Reuss–Hill approximation in the present work (PW), in addition to listing the average and standard deviation values. The Young's moduli, along $\langle 0001\rangle$ and $\langle 11\bar{2}0\rangle$, $E_{\langle 0001\rangle}$ and $E_{\langle 11\bar{2}0\rangle}$, respectively, the Ledbetter–Migliori elastic anisotropy measure A^* [51], bulk modulus B and Poisson's ratios v_{12} ($= -\varepsilon_2/\varepsilon_1$), v_{13} ($= -\varepsilon_3/\varepsilon_1$), and v_{31} ($= -\varepsilon_1/\varepsilon_3$), calculated from the c_{ij} components, are also shown in Table 2. (Note that ε_i is an engineering strain component.) The elastic constants of single-crystalline ω phase (PW) at RT exhibited anisotropy of $c_{33} > c_{11}$, $c_{44} > c_{66}$ and $E_{\langle 0001\rangle} > E_{\langle 11\bar{2}0\rangle}$, reflecting the anisotropic hexagonal crystal structure. The elastic constants of ω phase at 0 K obtained by FP calculations based on DFT [29] also exhibited the same anisotropy of $c_{33} > c_{11}$ and $E_{\langle 0001\rangle} > E_{\langle 11\bar{2}0\rangle}$, although the FP calculations did not yield clear anisotropy for the shear moduli c_{44} and c_{66}. Note that, in the previous FP calculations [27–29], the evaluation of elastic properties was performed using the Vienna Ab Initio Simulation Package, and the exchange and correlation potentials were treated within the generalized gradient approximation of Perdew–Burke–Ernzerhof. Thus, the calculated elastic properties were almost the same among the previous FP calculations. For the elastic anisotropy, the Ledbetter–Migliori anisotropy measure A^* of the ω phase at RT (PW) was almost the same as that of the α phase at RT (Exp.). The Poisson's ratios of ω phase at RT (PW) exhibited anisotropy, and the relationship between the magnitudes of v_{12}, v_{13} and v_{31} was the same as that of the α phase at RT (Exp.), even though the atomic positions in the hexagonal unit cells were different between them. The present bulk modulus value of 111.9 GPa for the ω phase at RT was almost the same as the previously measured value of 115 GPa [18].

To examine the validity of the c_{ij} components in the single-crystalline ω phase calculated by the inverse Voigt–Reuss–Hill approximation, the elastic stiffness of the textured ω-phase polycrystal was calculated from the single-crystalline c_{ij} using the "normal" Voigt–Reuss–Hill approximation. The calculated elastic stiffness components of the textured ω-phase polycrystal (PC; Calc) were compared with the measured components (PC; Meas), as shown in Table 1; the normal Voigt–Reuss–Hill approximation was applied to the averages of single-crystalline c_{ij} components. The calculated elastic stiffness components of the ω-phase polycrystal (PC; Calc) were almost the same as the averages of the measured components (PC; Meas). Hence, the application of the Voigt–Reuss–Hill approximation, followed by the application of the inverse Voigt–Reuss–Hill approximation to the polycrystalline c_{ij} of the ω phase, yielded values that were almost identical to the original polycrystalline c_{ij} values. This indicates the validity of the calculated single-crystalline c_{ij} on the assumption adopted in the Voigt–Reuss–Hill approximation.

Table 2
Elastic stiffness components c_{ij} (GPa), Young's moduli along $\langle 0001\rangle$ and $\langle 11\bar{2}0\rangle$, i.e., $E_{<0001>}$ and $E_{\langle 11\bar{2}0\rangle}$ (GPa), respectively, the Ledbetter–Migliori elastic anisotropy measure A^* [51], bulk modulus B (GPa) and Poisson's ratios of v_{12}, v_{13}, and v_{31} of single-crystalline ω phase determined by the experiments (Exp.) at RT in the present work (PW) and FP calculations based on DFT [29]. $c_{66} = (c_{11} - c_{12})/2$ and $A^* = v_2^2/v_1^2$, where v_1 and v_2 denote the minimum and maximum shear sound-wave velocities among all propagation directions [51]. E_{iso} (GPa), G_{iso} (GPa) and v_{iso} (GPa) are the Young's modulus, shear modulus and Poisson's ratio of the isotropic polycrystal. The elastic constants of α and β phases of Ti determined by experiments [38–40] and FP calculations based on DFT [29] are shown for comparison. For the ω phase at RT, the standard deviations reflect the variations in c_{11}, c_{12} and c_{13} for four polycrystalline ω-phase specimens to which the inverse Voigt–Reuss–Hill approximation was applied. The c_{33} and c_{44} components of the polycrystalline ω phase were fixed as their average values in the application of the inverse Voigt–Reuss–Hill approximation.

Phase	Temp. (K)	c_{11}	c_{33}	c_{12}	c_{13}	c_{44}	c_{66}	$E_{<0001>}$	$E_{\langle 11\bar{2}0\rangle}$	Method
ω	RT	178.9 ± 0.3	228.4 ± 7.4	90.2 ± 4.5	60.8 ± 0.6	70.5 ± 3.2	44.4 ± 2.1	201.0 ± 7.4	129.0 ± 3.9	Exp. (PW)
ω	0	194	245	81	54	54	56.5	224	156	FP [29]
α	RT	162.4	180.7	92.0	69.0	46.7	35.2	143.3	104.4	Exp. [38]
α	4	176.1	190.5	86.9	68.3	50.8	44.6	155.0	125.9	Exp. [38]
α	0	172	190	82	75	45	45	123	146	FP [29]
β	1293	134		110		36				Exp. [40]
β	1273	97.7		82.7		37.5				Exp. [39]

Phase	Temp. (K)	A^*	B	v_{12}	v_{13}	v_{31}	E_{iso}	G_{iso}	v_{iso}	Method
ω	RT	1.6 ± 0.1	111.9 ± 0.8	0.45 ± 0.02	0.14 ± 0.00	0.23 ± 0.00	152.8 ± 0.6	60.1 ± 0.3	0.27 ± 0.00	Exp. (PW)
ω	0	1.5	112	0.38	0.14	0.20	155	61	0.27	FP [29]
α	RT	1.5	107.3	0.48	0.20	0.27	114.6	43.4	0.32	Exp. [38]
α	4	1.3	110.0	0.41	0.21	0.26	130.6	50.2	0.30	Exp. [38]
α	0	1.0	111	0.37	0.25	0.30	123	47	0.31	FP [29]
β	1293	3.0	118	0.45	0.45	0.45	65	23	0.41	Exp. [40]
β	1273	5.0	87.7	0.46	0.46	0.46	55	20	0.39	Exp. [39]

4.3. Comparison with FP calculations and elastic properties of the α phase

4.3.1. Young's modulus

To examine the crystallographic elastic anisotropy of the single-crystalline ω phase in detail, the dependence of the Young's modulus on the crystallographic orientation was calculated by coordinate conversion of the single-crystalline c_{ij} components [46,49]. Fig. 5a shows the Young's modulus of the ω phase at RT between the ⟨0001⟩ and ⟨11$\bar{2}$0⟩ directions, which was obtained from the experiments (Exp.) in the present study. The symbol θ denotes the angle from the ⟨0001⟩ direction. The line and error bars denote the average Young's modulus and standard deviations, respectively. The Young's moduli of the α phase at RT obtained in the experiments (Exp.) [38] are shown for the sake of comparison. Interestingly, at RT, the Young's modulus of the metastable ω phase was higher than that of the stable α phase in all the crystallographic directions. When one focused on the orientation dependence, the Young's modulus of the ω phase monotonically decreased with an increase in the angle θ. Consequently, the Young's modulus in the ⟨0001⟩ direction was the highest, which was similar to the orientation dependence of the Young's modulus in the α phase.

The orientation dependence of the Young's modulus in the ω phase at RT, obtained by experiments, as shown in Fig. 5a, was compared with that at 0 K obtained by FP calculations [29], shown in Fig. 5b. The orientation dependence of the Young's modulus in the ω phase at 0 K (FP) was almost similar to that shown in the experiments (Exp.) at RT, even though the Young's modulus (FP) exhibited a minimum at ~55°. Similarly, the Young's modulus of the α phase at 0 K (FP) showed a minimum at ~57°, as shown in Fig. 5b, whereas the Young's modulus of the α phase (Exp.) at 4 K in Fig. 5b and RT in Fig. 5a did not exhibit such a clear minimum.

4.3.2. Shear modulus

The dependence of the shear modulus on the crystallographic orientation was also examined. Fig. 6a shows the shear moduli of the ω and α phases at RT between the {0001}⟨11$\bar{2}$0⟩ and {11$\bar{2}$0}⟨0001⟩ shear directions. θ denotes the angle from the {0001}⟨11$\bar{2}$0⟩ shear direction. At RT, the shear modulus of the metastable ω phase (Exp.) was higher than that of the stable α phase (Exp.), as in the case of the Young's modulus. The shear modulus of the ω phase monotonically decreased with an increase in θ, consistent with the shear modulus of the α phase at RT. The shear modulus of α phase at 4 K (Exp.) also exhibited similar anisotropy, as shown in Fig. 6b. However, the shear modulus of ω and α phases at 0 K (FP) did not exhibit such anisotropy, as shown in Fig. 6b. This indicates that the elastic properties yielded by the FP calculations were slightly different from the experimental values, especially for the shear modulus. It should be noted that, for the ω phase, part of the difference in the elastic properties between the measurements and FP calculations could possibly have been caused by the difference in the temperature between them. In the FP calculations, the elastic properties were calculated on the basis of the ground-state electronic structures. Thus, the calculated elastic stiffness corresponded to the stiffness at 0 K, which is generally different from that at RT because of the absence of the effect of anharmonic lattice vibrations [52].

4.4. Possible mechanism of high elastic modulus of ω phase

For the ω, α and β phases in Ti, the Young's modulus E_{iso}, shear modulus G_{iso} and Poisson's ratio ν_{iso} of the isotropic polycrystal were calculated from their single-crystal c_{ij} values, using the orientation average based on the Voigt–Reuss–Hill approximation [46,47]. The calculated values are shown in Table 2. The Young's modulus E_{iso}

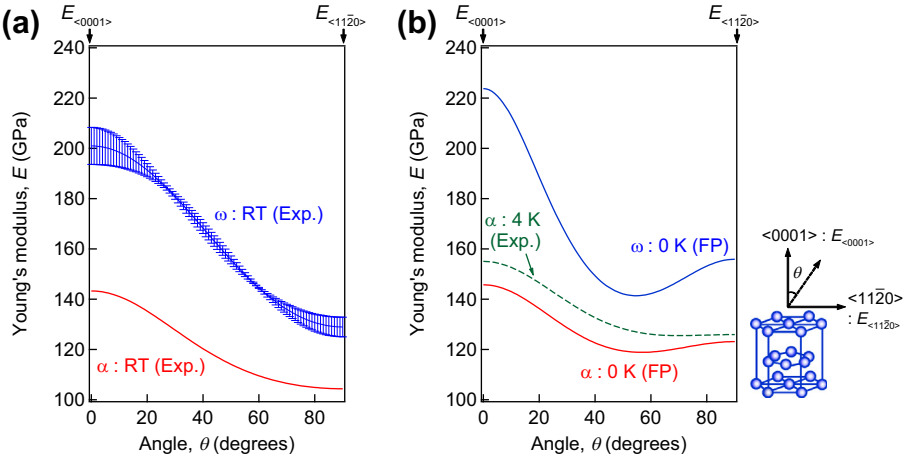

Fig. 5. Dependence of the Young's modulus on the crystallographic orientation in single-crystalline ω phase between the ⟨0001⟩ and ⟨11$\bar{2}$0⟩ directions at (a) RT and (b) 0 K, which were obtained by experiments (Exp.) and FP calculations [29], respectively. θ is the angle from the ⟨0001⟩ direction. The lines and error bars denote the average and standard deviation values, respectively. The Young's modulus of the α phase at (a) RT and (b) 4 K obtained by experiments (Exp.) [38] and (b) the Young's modulus at 0 K obtained by FP calculations [29] are shown for comparison.

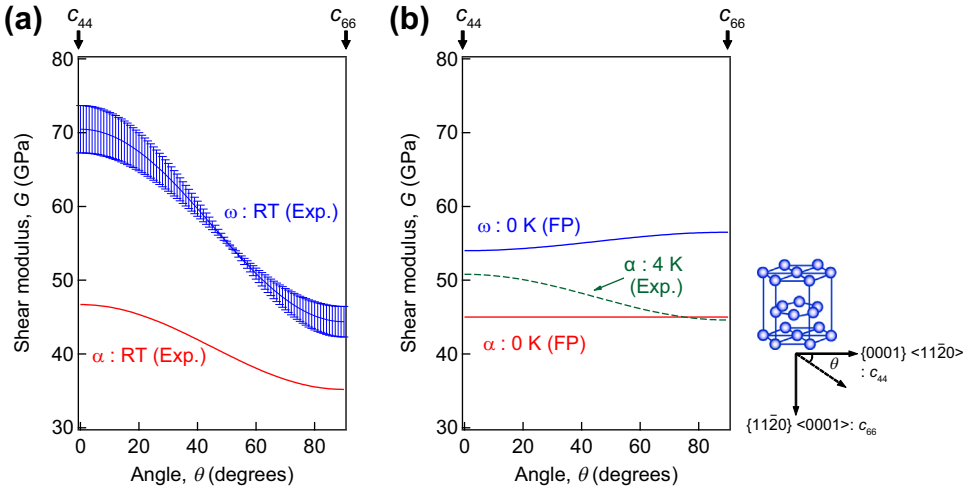

Fig. 6. Dependence of the shear modulus on the crystallographic orientation in single-crystalline ω phase between the $\{0001\}\langle 11\bar{2}0\rangle$ and $\{11\bar{2}0\}\langle 0001\rangle$ shear directions at (a) RT and (b) 0 K, which were obtained by experiments (Exp.) and FP calculations [29], respectively. θ is the angle from the $\{0001\}\langle 11\bar{2}0\rangle$ shear direction. The lines and error bars denote the average and standard deviation values, respectively. The shear modulus of the α phase at (a) RT and (b) 4 K obtained by experiments (Exp.) [38] and (b) the shear modulus at 0 K obtained by FP calculations [29] are shown for comparison.

and shear modulus G_{iso} of the ω phase at RT (PW) were clearly higher than those of the β phase at high temperatures of 1273 and 1293 K, as is expected from the previous studies for Ti alloys [16,25,26,13]. Importantly, the Young's modulus E_{iso} and shear modulus G_{iso} of the metastable ω phase were also clearly higher than those of α phase stable at RT.

This peculiar relationship in the magnitudes of the elastic moduli between the metastable ω and stable α phases could possibly be related to the stabilization mechanism of the α phase. Various models based on the FP calculations [3–5,27,53] have suggested that the true zero-temperature ground state is not the α phase, but the ω phase (i.e., the binding energy of the ω phase is higher than that of the α phase at 0 K), even though the ω phase state is not realized at 0 K because of the high energy barrier for the α to ω transformation. At RT, entropy from the thermal population of phonons stabilizes the α phase, even though the enthalpy of the ω phase is lower than that of the α phase [3]. This thermodynamical relationship between the α and ω phases is now generally accepted [5].

At 0 K, the elastic stiffness corresponds to the second derivative of internal energy (i.e., the curvature of binding energy) with respect to a strain component measured from the equilibrium atom positions. Thus, the high binding energy of the ω phase probably results in the high elastic modulus of ω phase at 0 K, which explains the FP calculation results in Table 2. At RT, the entropy from the thermal population of phonons stabilizes the α phase rather than the ω phase; however, it possibly does not alter the binding state of the ω phase much. Thus, the elastic modulus of the ω phase is possibly high even at RT.

4.5. Effect of severe plastic deformation on the elastic modulus of the ω phase

In general, severe plastic deformation introduces many dislocations [54,55], which usually lower the elastic stiffness [56,57]. The ω phase formed by the HPT process contained many dislocations, as shown in Fig. 1a, which possibly lowered the elastic stiffness, although the effect cannot be evaluated precisely within the scope of the present study.

5. Micromechanics analysis to explain the effect of ω-phase formation on the elastic properties of β-phase titanium alloys

5.1. Micromechanics model

For β-phase Ti–Cr and Ti–V alloys with low β-phase stability, the effect of the formation of athermal or deformation-induced ω phase on the elastic properties was evaluated by micromechanics modeling, using the elastic stiffness of the ω-phase single crystal. In the calculation of the model, a β-phase Ti alloy single crystal containing the ω phase was approximated as a composite material consisting of a matrix of the β-phase single crystal and inclusions of ω-phase single crystal. Note that the four ω-phase variants with the actual crystallographic orientation relationships of $(0001)_\omega // \{111\}_\beta$ and $\langle 11\bar{2}0\rangle_\omega // \langle 1\bar{1}0\rangle_\beta$ [24] were taken into account.

The effective (macroscopic) elastic stiffness of a composite material consisting of a matrix and inclusions can be calculated using various micromechanics models [58,59]. In the present study, a micromechanics model termed the "effective-mean-field" (EMF) theory [41] based on Eshelby's inclusion theory [42], Mori–Tanaka's mean-field theory [43] and Bruggeman's effective-medium approxima-

tion [44] was used. This is because the EMF theory yields reasonable elastic properties for a composite material in which the elastic stiffness of the inclusions is significantly different from that of the matrix phase.

In the EMF theory, first, the effective elastic stiffness $\overline{\mathbf{C}}_{(1)}$ of a composite material containing a small fraction $\Delta f \ll 1$ of inclusions is calculated on the basis of Mori–Tanaka's mean-field theory and Eshelby's inclusion theory. The bold face capital indicates a 6×6 matrix. Then, the composite material is approximated as a homogeneous material with the effective elastic stiffness of $\overline{\mathbf{C}}_{(1)}$ based on the effective-medium approximation. Next, the effective elastic stiffness $\overline{\mathbf{C}}_{(2)}$ of a composite material containing inclusions with the volume fraction of $2\Delta f$ is calculated by adding the inclusions of Δf to the homogeneous material with the effective elastic stiffness of $\overline{\mathbf{C}}_{(1)}$. This calculation is repeated sequentially until the volume fraction of the inclusions reaches an objective value. In this sequential calculation, Mori–Tanaka's mean-field theory is virtually applied to composite materials with a small fraction of inclusions. Thus, the EMF theory gives a better effective elastic stiffness than the conventional Mori–Tanaka mean-field theory [41,60].

On the basis of the EMF theory, the effective elastic stiffness $\overline{\mathbf{C}}_{(n+1)}$ of the alloy consisting of a β-phase matrix and ω-phase inclusions with a fraction of $f_\omega = (n+1)\Delta f$ is given by the following sequential calculations from $n = 0$ to $n = N - 1$ [60].

$$\overline{\mathbf{C}}_{(n+1)} = \overline{\mathbf{C}}_{(n)} + \frac{\Delta f}{1 - n\Delta f}[\langle \mathbf{C}_\mathrm{I}\mathbf{A}^{\mathrm{MT}}_{(n)}\rangle - \overline{\mathbf{C}}_{(n)}\langle \mathbf{A}^{\mathrm{MT}}_{(n)}\rangle]. \tag{7}$$

In the above equation, $\overline{\mathbf{C}}_{(0)}$ and $\mathbf{C}_\mathrm{I}$ are the elastic stiffness values of the β-phase matrix and the ω-phase inclusion. $\langle\rangle$ indicates the average for the four ω variants [58]. $\Delta f = 1/N \ll 1$, where N is the number of sequential calculations; in the present case, sequential calculations of $N = 100$ were sufficient for the convergence of $\overline{\mathbf{C}}_{(n+1)}$. The matrices $\langle \mathbf{C}_\mathrm{I}\mathbf{A}^{\mathrm{MT}}_{(n)}\rangle$ and $\langle \mathbf{A}^{\mathrm{MT}}_{(n)}\rangle$ are given by

$$\langle \mathbf{C}_\mathrm{I}\mathbf{A}^{\mathrm{MT}}_{(n)}\rangle = \left\langle \mathbf{C}_\mathrm{I}\mathbf{A}^{\mathrm{dil}}_{(n)}\left[\left(1 - \frac{\Delta f}{1 - n\Delta f}\right)\mathbf{I} + \frac{\Delta f}{1 - n\Delta f}\mathbf{A}^{\mathrm{dil}}_{(n)}\right]^{-1}\right\rangle, \tag{8}$$

and

$$\langle \mathbf{A}^{\mathrm{MT}}_{(n)}\rangle = \left\langle \mathbf{A}^{\mathrm{dil}}_{(n)}\left[\left(1 - \frac{\Delta f}{1 - n\Delta f}\right)\mathbf{I} + \frac{\Delta f}{1 - n\Delta f}\mathbf{A}^{\mathrm{dil}}_{(n)}\right]^{-1}\right\rangle, \tag{9}$$

respectively, where

$$\mathbf{A}^{\mathrm{dil}}_{(n)} = \left[\mathbf{S}_{(n)}\overline{\mathbf{C}}^{-1}_{(n)}(\mathbf{C}_\mathrm{I} - \overline{\mathbf{C}}_{(n)}) + \mathbf{I}\right]^{-1}, \tag{10}$$

and $\mathbf{I}$ is the unit matrix. $\mathbf{S}_{(n)}$ is the matrix notation of the Eshelby tensor, which depends on the elastic stiffness of the matrix phase $\overline{\mathbf{C}}_{(n)}$ and the shape of the inclusions [46,61].

In the present calculation, the elastic stiffness of the β phase in Ti–9.36Cr [13] (Table 3) and Ti–28V [62] (at.%) alloys measured in previous studies were used as the elastic stiffness values of matrix phases. The ω phases were approximated as spherical inclusions, because it was difficult to determine the detailed morphology for the deformation-induced and athermal ω phases compared with that of the isothermal ω phase [63]. The elastic stiffness components of the ω phase in the Ti–Cr and Ti–V alloys were approximated as those of the ω phase in Ti, which were determined in the present study. In reality, the additions of Cr and V probably affect the elastic stiffness of the ω phase, even though the effects may be insignificant when the concentrations of Cr and V are low. Note that, while the present evaluation by the micromechanics model contains some approximations, the present authors believe that the analysis for the effect of ω-phase formation on the elastic properties is helpful for understanding the elastic properties of Ti alloys, especially those developed for biomedical applications.

5.2. Calculated results

5.2.1. Elastic properties of single crystals

The calculated c_{ij} of the Ti–Cr and Ti–V alloy single crystals consisting of a β-phase matrix and ω-phase inclusions exhibited cubic elastic symmetry because of the equivalent distributions of the four ω-phase variants. From the calculated c_{ij} components, three important elastic constants for cubic elastic symmetry were obtained; the shear modulus $c' = (c_{11} - c_{12})/2$, the anisotropy factor $A = c_{44}/c'$ and the bulk modulus $B = (c_{11} + 2c_{12})/3$. Fig. 7a shows the shear modulus c' as a function of the volume fraction of the ω phase f_ω. For both the Ti–Cr and Ti–V alloys, the shear modulus c' increased with an increase in f_ω, reflecting the large elastic modulus of the ω phase. The shear modulus c_{44} in both the alloys also increased with increasing f_ω, as shown in Fig. 7b. However, the anisotropy factor $A(= c_{44}/c')$ decreased with increasing f_ω, as shown in Fig. 7c. Hence, the shear modulus c' was more sensitively enhanced by the ω-phase formation than the shear modulus c_{44}. In contrast to the shear moduli c' and c_{44}, the bulk

Table 3
Shear modulus c' (GPa), shear modulus c_{44} (GPa), anisotropy factor $A(= c_{44}/c')$ and bulk modulus B (GPa) of β-phase Ti–6.98Cr (at.%) alloy single crystal with athermal ω-phase and β-phase Ti–9.36Cr (at.%) alloy single crystal without the ω phase [13]. The two single crystals are denoted as $\beta + \omega$ and β phases, respectively. Young's moduli $E_{\beta+\omega}$ and E_β (GPa) of the β-phase Ti–9.3Cr and Ti–21.0V (at.%) alloy polycrystals with and without the ω phase, respectively, are also shown [26,65]. The ω phase was formed by cold working, and the Ti–9.3Cr alloy contained a small amount of athermal ω phase before cold working, even though it virtually consisted of a β phase.

	c'	c_{44}	A	B
Ti–6.98Cr ($\beta + \omega$)	36.7	55.4	1.5	107.0
Ti–9.36Cr (β)	19.0	42.7	2.2	107.8
		$E_{\beta+\omega}$		E_β
Ti–9.3Cr		92.5		82.5
Ti–21.0V		85		75

modulus was insensitive to the volume fraction of the ω phase, as shown in Fig. 7d.

To compare with the calculation results, the shear modulus c', shear modulus c_{44}, anisotropy factor A and bulk modulus B of the β-phase Ti–Cr alloys with and without the athermal ω phase [13] are shown in Table 3. The volume fraction of the ω phase was not analyzed in the previous study [13] because the measurement of the nanosized ω phase was generally difficult. Thus, the focus is only on the relationship between the magnitudes of the elastic constants of the alloys with and without the ω phase. The shear moduli c' and c_{44} of the Ti–6.98Cr alloy with the ω phase ($\beta + \omega$ phases) are higher than those of the Ti–9.36 alloy consisting of a β phase (β phase), as shown in Table 3. However, the anisotropy factor A of the $\beta + \omega$ phases was lower than that of the β phase. These relationships between the elastic constants of the alloys with and without the ω phase are consistent with the results of the calculations shown in Fig. 7a–c. Table 3 also indicates that the bulk modulus remains unchanged by the formation of the ω phase, which coincides with the calculation result shown in Fig. 7d. Also for the quaternary Ti–Nb–Ta–Zr alloys, the ω-phase formation increased the c' and c_{44} values and decreased the A value [64], in agreement with the results of the present calculation.

5.2.2. Young's modulus of the polycrystal

Fig. 8 shows the micromechanics calculations for the Young's modulus of the Ti–Cr and Ti–V alloy isotropic polycrystals as a function of f_ω; the Young's modulus of the isotropic polycrystal was calculated from the elastic constants of the corresponding single crystal on the basis of the Voigt–Reuss–Hill approximation [47] by Eq. (11).

$$E_{\mathrm{iso}} = \frac{1}{2}\left\{\frac{9}{1/B + 15/(2c' + 3c_{44})} + \frac{5}{5/(9B) + 2/(3c') + 1/c_{44}}\right\}. \tag{11}$$

The Young's modulus increased with an increase in the f_ω, as expected. For comparison, the Young's moduli of the β-phase Ti–9.3Cr and Ti–21.0V (at.%) alloys with and without deformation-induced ω phase [26,65] are shown in Table 3. The Young's modulus of the alloy with the ω

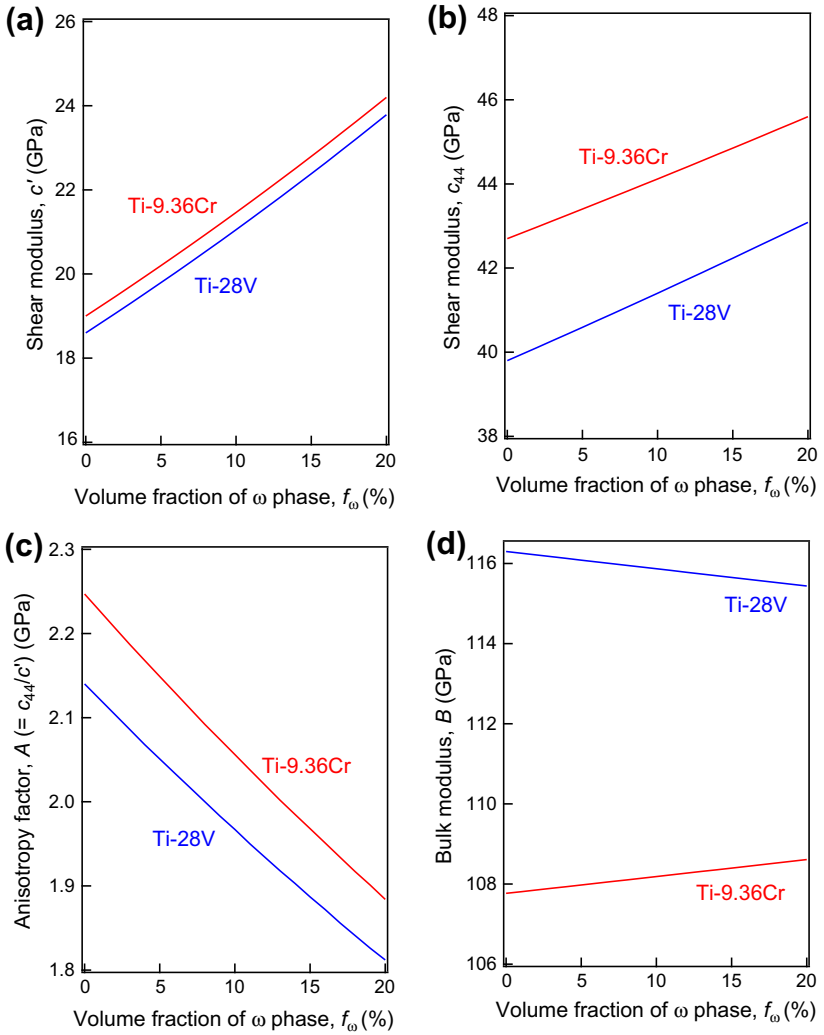

Fig. 7. Micromechanics calculations for elastic constants of Ti–9.36Cr and Ti–28V (at.%) alloy single crystals consisting of β and ω phases as a function of f_ω: (a) shear modulus c'; (b) shear modulus c_{44}; (c) anisotropy factor A; and (d) bulk modulus B.

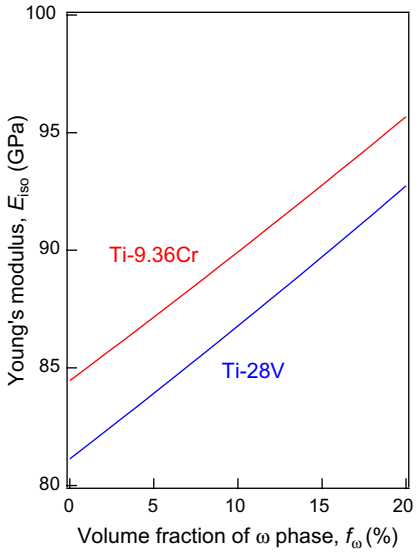

Fig. 8. Micromechanics calculations for the Young's modulus of Ti–9.36Cr and Ti–28V (at.%) alloy isotropic polycrystals consisting of β and ω phases, as a function of f_ω.

phase ($E_{\beta+\omega}$) was higher than that consisting of a β phase (E_β) in both Ti–Cr and Ti–V alloys. This coincided with the results of the calculations, as shown in Fig. 8. Importantly, Eq. (11) indicates that the increases in c' and c_{44} contribute markedly to the increase in the Young's modulus of the polycrystal, whereas the contribution from the increase in B is small. Therefore, it can be deduced that the ω-phase formation increases the shear moduli c' and c_{44} of the β-phase Ti alloy single crystals, causing an increase in the Young's modulus of the polycrystal.

The micromechanics model using the single-crystalline elastic stiffness of the ω phase deduced the effect of the ω-phase formation on the elastic properties in β-phase Ti alloys and explained the previous experimental results for the change in the elastic properties caused by the ω-phase formation. For a more detailed analysis, the present authors intend to clarify the effect of alloying elements on the elastic properties of the ω phase in the future.

6. Conclusions

The elastic properties of single-crystalline ω (hexagonal) phase of titanium were studied. Disk specimens consisting of a single phase of the ω-phase polycrystal were prepared by HPT processing. For the ω-phase polycrystal, a complete set of elastic constants was measured by RUS combined with LDI and EMAR. By analyzing the elastic stiffness of the ω-phase polycrystal on the basis of an inverse Voigt–Reuss–Hill approximation, the elastic stiffness components of the single-crystalline ω phase were determined. Furthermore, the effect of the formation of the ω phase on the elastic properties of β-phase titanium alloys was analyzed by a micromechanics model termed the EMF theory, using the elastic stiffness of the ω phase determined.

(i) A disk specimen consisting of ω-phase polycrystal prepared by the HPT process, possessed a strong texture; the $\langle 10\bar{1}0\rangle_\omega$ and/or $\langle 11\bar{2}0\rangle_\omega$ directions of the ω-phase crystals were strongly oriented along the thickness (x_3) direction, whereas the $\langle 0001\rangle_\omega$ directions were isotropically oriented in the plane perpendicular to the thickness direction. As a result, the ω-phase polycrystal exhibited hexagonal elastic symmetry macroscopically.

(ii) The Young's modulus of the single-crystalline ω phase along the $\langle 0001\rangle$ direction was clearly higher than that along the $\langle 11\bar{2}0\rangle$ direction, and the shear modulus for the $\{0001\}\langle 11\bar{2}0\rangle$ shear direction (c_{44}) was higher than that for the $\{11\bar{2}0\}\langle 0001\rangle$ shear direction (c_{66}). The elastic stiffness components of the single-crystalline ω phase determined by the inverse Voigt–Reuss–Hill approximation were almost consistent with those estimated by previous FP calculations based on DFT, even though the FP calculations yielded slightly different shear moduli. The Young's modulus and shear modulus of the metastable ω phase were clearly higher than those of the α phase stable at room temperature. The Young's modulus and shear modulus of the ω phase at room temperature were also higher than those of the β phase at high temperatures.

(iii) From the micromechanics model, it could be deduced that the ω-phase formation increases the shear modulus c' and c_{44} of the β-phase Ti alloy single crystals, which causes an increase in the Young's modulus of the polycrystal. The shear modulus c' was more sensitively enhanced by the formation of the ω phase than the shear modulus c_{44}. These evaluations explained previous experimental results for the elastic properties of the β-phase Ti–Cr and Ti–V alloys with and without the ω phase.

Acknowledgments

This study was supported by a grant-in-aid for Scientific Research on Innovative Areas (Project "Materials Science on Synchronized LPSO Structure—The Evolution of the Material Science for Innovative Development of the Next Generation Lightweight Structure Materials") from the Ministry of Education, Culture, Sports, Science, and Technology of Japan (No. 24109505) and a research grant from the Light Metal Educational Foundation. Analyses by XRD and X-ray pole figure were performed at the Comprehensive Analysis Center, ISIR, Osaka University.

References

[1] Banerjee D, Williams JC. Acta Mater 2013;61:844.
[2] Hennig RG, Trinkle DR, Bouchet J, Srinivasan SG, Albers RC, Wilkins JW. Nat Mater 2005;4:129.
[3] Mei ZG, Shang SL, Wang Y, Liu ZK. Phys Rev B 2009;80:104116.

[4] Rudin SP, Jones MD, Albers RC. Phys Rev B 2004;69:4.
[5] Tegner BE, Zhu L, Ackland GJ. Phys Rev B 2012;85:214106.
[6] Raabe D, Sander B, Friák M, Ma D, Neugebauer J. Acta Mater 2007;55:4475.
[7] Kim HY, Wei L, Kobayashi S, Tahara M, Miyazaki S. Acta Mater 2013;61:4874.
[8] Geetha M, Singh AK, Asokamani R, Gogia AK. Prog Mater Sci 2009;54:397.
[9] Niinomi M. Biomaterials 2003;24:2673.
[10] Zhang YW, Li SJ, Obbard EG, Wang H, Wang SC, Hao YL, et al. Acta Mater 2011;59:3081.
[11] Elias LM, Schneider SG, Schneider S, Silva HM, Malvisi F. Mater Sci Eng A 2006;432:108.
[12] Talling RJ, Dashwood RJ, Jackson M, Kuramoto S, Dye D. Scr Mater 2008;59:669.
[13] Fisher ES, Dever D. Acta Metall 1970;18:265.
[14] Ikehata H, Nagasako N, Furuta T, Fukumoto A, Miwa K, Saito T. Phys Rev B 2004;70:174113.
[15] Tane M, Akita S, Nakano T, Hagihara K, Umakoshi Y, Niinomi M, et al. Acta Mater 2010;58:6790.
[16] Tane M, Nakano T, Kuramoto S, Hara M, Niinomi M, Takesue N, et al. Acta Mater 2011;59:6975.
[17] Vohra YK, Spencer PT. Phys Rev Lett 2001;86:3068.
[18] Kerley GI. Sand Rep 2003;3785:1.
[19] Ahuja R, Dubrovinsky L, Dubrovinskaia N, Guillen JMO, Mattesini M, Johansson B, et al. Phys Rev B 2004;69:184102.
[20] Ramsteiner IB, Shchyglo O, Mezger M, Udyansky A, Bugaev V, Schöder S, et al. Acta Mater 2008;56:1298.
[21] Dutta J, Ananthakrishna G, Banerjee S. Acta Mater 2012;60:556.
[22] Devaraj A, Nag S, Srinivasan R, Williams REA, Banerjee S, Banerjee R, et al. Acta Mater 2012;60:596.
[23] Nag S, Zheng Y, Williams REA, Devaraj A, Boyne A, Wang Y, et al. Acta Mater 2012;60:6247.
[24] Sikka SK, Vohra YK, Chidambaram R. Prog Mater Sci 1982;27:245.
[25] Tane M, Nakano T, Kuramoto S, Niinomi M, Takesue N, Nakajima H. Acta Mater 2013;61:139.
[26] Zhao X, Niinomi M, Nakai M, Hieda J, Ishimoto T, Nakano T. Acta Biomater 2012;8:2392.
[27] Hu C-E, Zeng Z-Y, Zhang L, Chen X-R, Cai L-C, Alfe D. J Appl Phys 2010;107:093509.
[28] Hao YJ, Zhang L, Chen XR, Li YH, He HL. Solid State Commun 2008;146:105.
[29] Trinkle DR, Jones MD, Hennig RG, Rudin SP, Albers RC, Wilkins JW. Phys Rev B 2006;73:054121.
[30] Kilmametov AR, Khristoforov AV, Wilde G, Valiev RZ. Z Kristallogr Suppl 2007;2:339.
[31] Todaka Y, Sasaki J, Moto T, Umemoto M. Scr Mater 2008;59:615.
[32] Ivanisenko Y, Kilmametov A, Rösner H, Valiev RZ. Int J Mater Res 2008;99:36.
[33] Edalati K, Matsubara E, Horita Z. Metall Mater Trans A 2009;40:2079.
[34] Ohno I. J Phys Earth 1976;24:355.
[35] Ogi H, Sato K, Asada T, Hirao M. J Acoust Soc Am 2002;112:2553.
[36] Hirao M, Ogi H, Fukuoka H. Rev Sci Instrum 1993;64:3198.
[37] Tane M, Nagai Y, Kimizuka H, Hagihara K, Kawamura Y. Acta Mater 2013;61:6338.
[38] Fisher ES, Renken CJ. Phys Rev 1964;135:A482.
[39] Ledbetter M, Ogi H, Kai S, Kim S, Hirao M. J Appl Phys 2004;95:4642.
[40] Petry W, Heiming A, Trampenau J, Alba M, Herzig C, Schober HR, et al. Phys Rev B 1991;43:10933.
[41] Tane M, Ichitsubo T. Appl Phys Lett 2004;85:197.
[42] Eshelby JD. Proc R Soc Lond A 1957;241:376.
[43] Mori T, Tanaka K. Acta Metall 1973;21:571.
[44] Bruggeman DAG. Ann Phys (Leipzig) 1935;24:636.
[45] Kim S, Ledbetter H, Ogi H. J Appl Phys 2000;88:2378.
[46] Mura T. Micromechanics of defects in solids. 2nd rev. ed. The Hague: Martinus Nijhoff; 1987. p. 133–14 and 423.
[47] Hill R. Proc Phys Soc A 1952;65:349.
[48] Voigt W. Ann Phys – Berlin 1889;38:954.
[49] Nye JF. Physical properties of crystals: their representation by tensors and matrices. New York: Oxford University Press; 1984. p. 131–5.
[50] Reuss AZ. Angew Math Mech 1929;8:55.
[51] Ledbetter H, Migliori A. J Appl Phys 2006;100:063516.
[52] Grimvall G. Thermophysical properties of materials, enlarged and rev. ed. New York: Elsevier; 1999. p. 57–60.
[53] Ostanin SA, Trubitsin VY. J Phys: Condens Matter 1997;9:L491.
[54] Valiev RZ, Islamgaliev RK, Alexandrov IV. Prog Mater Sci 2000;45:103.
[55] Zhilyaev AP, Langdon TG. Prog Mater Sci 2008;53:893.
[56] Ledbetter HM, Kim SA. Mater Sci Eng 1988;101:87.
[57] Benito JA, Manero JM, Jorba J, Roca A. Metall Mater Trans A 2005;36:3317.
[58] Dunn ML, Ledbetter H, Heyliger PR, Choi CS. J Mech Phys Solids 1996;44:1509.
[59] Christensen RM. J Mech Phys Solids 1990;38:379.
[60] Tane M, Ichitsubo T, Nakajima H, Hyun SK, Hirao M. Acta Mater 2004;52:5195.
[61] Kinoshita N, Mura T. Phys Status Solidi 1971;A5:759.
[62] Fisher ES. Review of solute effects on the elastic moduli of bcc transition metals. In: Collings EW, Gegel HL, editors. Physics of solid solution strengthening. New York: Plenum Press; 1975. p. 265.
[63] Hickman BS. J Mater Sci 1969;4:554.
[64] Tane M, Akita S, Nakano T, Hagihara K, Umakoshi Y, Niinomi M, et al. Acta Mater 2008;56:2856.
[65] Zhao X, Niinomi M, Nakai M, Hieda J. Mater Trans 2012;53:1379.